HHS Public Access

Author manuscript

J Biophotonics. Author manuscript; available in PMC 2018 June 01.

Published in final edited form as:

J Biophotonics. 2017 June ; 10(6-7): 799–804. doi:10.1002/jbio.201600151.

Second generation slit-based photoacoustic tomography system for vascular imaging in human

Yuehang Wang, **Depeng Wang**, **Ryan Hubbell**, and **Jun Xia***

Department of Biomedical Engineering, University at Buffalo North Campus, Buffalo, New York 14260, USA

Abstract

Slit-based photoacoustic tomography is a newly developed technique that improves the elevation numerical aperture of a linear array through acoustic diffraction. The slit, placed at the acoustic focus of a linear array, effectively forms an array of virtual detectors with high receiving angle, which subsequently improves the elevation resolution. However, due to the complex implementation, our original system could only image phantoms and sacrificed animals. In this report, the system has been significantly improved. In particular, we designed a slit holder that can be directly mounted to the transducer array for easy adjustment of slit width and simultaneous scanning of both the array and the slit. To enlarge the imaging field of view, we replaced the single circular optical fiber bundle with a bifurcated line fiber bundle which moved simultaneously with the array and the slit. The data acquisition system has also been updated to double the imaging speed. With these improvements, the new system can image a 3.8 × 4 cm^2 region within 40 seconds and the object only needs to be coupled through ultrasound gel. We successfully used the system to image vasculatures in the palm and forearm of human volunteers.

Graphical Abstract

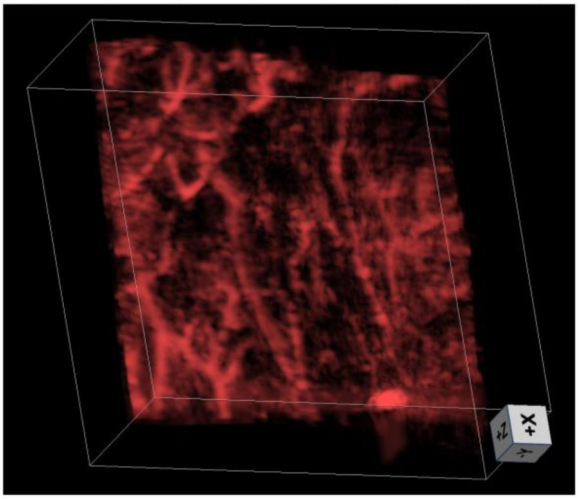

3D palm vascular image of human palm

*Corresponding author: junxia@buffalo.edu.

Keywords

photoacoustic tomography; slit-based; vascular imaging; three dimensional imaging

1. Introduction

Over the past few years, linear-array-based photoacoustic tomography (PAT) systems have been drawing increasing interest due to their low cost and easy integration with existing ultrasound systems [1–7]. However, a linear array is known to be suited for only two dimensional (2D) imaging due to the intrinsic poor elevation resolution. In most 3D linear array images, the elevation feature looks blurry compared to lateral or axial features [8]. Multiple methods have been proposed to address this issue through different scanning geometries [5, 9] or advanced image reconstruction techniques [10]. Recently, we proposed a unique method to address this limitation based on acoustic diffraction through a thin slit, which was placed at the acoustic focus of the linear array [11]. The acoustic diffraction greatly increases the elevation receiving aperture of the array and hence improves the corresponding spatial resolution. In our initial study, the method has been demonstrated to work well on phantoms and animals *in situ*. The spatial resolution of the system is near isotropic in all three dimensions (0.144 mm axial, 0.298 mm lateral, and 0.33 mm elevational). However, because our preliminary system was designed in a way that the transducer and the slit were fixed while the object was fully immersed in water and scanned inside a water tank, *in vivo* imaging was difficult to be implemented. In addition, we just chose a slit width corresponding to the wavelength of the central frequency of the array. However, unlike conventional optical imaging, the photoacoustic frequency spectrum is determined by the object and it typically contains a wide range of acoustic frequencies (wavelengths). Thus the slit width should be adjustable based on features of the object. These issues are addressed in this study. As will be seen in the following section, our new system has a more convenient imaging geometry and can be easily used to image phantoms and human palms and forearms.

2. Methods

Figure 1 compares the designs of our first and second generation slit PAT systems. In the original system (Fig. 1a), the transducer, slit and object were all immersed in water and the object was scanned in the vertical direction for 3D imaging. Imaging of objects *in vivo* could be challenging in this design. For the updated system shown in Fig. 1b, we designed an open-bottom water tank and submerged only the transducer and slit in water. The scanning direction was also changed from vertical to horizontal, as identified by double arrows. The bottom of the water tank was sealed with 0.05 mm thickness FEP plastic film (85905K64, McMASTER-Carr) and the object could be imaged through this window. FEP plastic was chosen here due to its high strength and transparent color. We also optimized the slit material. In our original system, the slit was made by two iron blades, this metal material became rusty after immersion in water and it required frequent cleaning. In the updated system, the slit was formed by two 316 stainless steels (2317K58, McMASTER-Carr). This type of steel has excellent corrosion resistance and is designed to be used in marine

applications. The two steel sheets have a thickness of 0.3 mm which is a quarter of the acoustic wavelength in stainless steel (1.2 mm). This thickness minimizes the transmitted sound energy [12]. We also designed an array holder to mount the two steel sheets in front of the transducer array. In the holder, both steel sheets are compressed by a set of screws. The slit width can be easily adjusted by loosening the screws. In order to quickly reach the desired slit width, we machined several aluminium sheets with thicknesses ranging from 0.3 mm to 2.4 mm with a step size of 0.3 mm. To adjust the slit width, we simply insert the corresponding aluminium sheet to the slit and align the two steel sheets to make a close fit and then tighten the locking screws.

Light illumination was provided by an Nd:YAG laser (Surelite SL III-10, Continuum) with <10 ns pulses width and 10 Hz pulse repetition frequency (PRF). 532 nm and 1064 nm output wavelengths were used for phantom and *in vivo* experiments, respectively. For light delivery, we used a bifurcated fiber bundle with a 1.1-cm-diameter circular input and two 5.1-cm-length line outputs (Light CAM #2, Schott Fostec). The beam on the object's surface was approximately 2.5 cm × 6.0 cm in size. Compared to the single circular fiber bundle in [11], the line fibers provide a more uniform illumination within the rectangular field of view. During the experiment, the fiber bundles were mounted on the slit holder and moved simultaneously with the transducer. While, in this design, the optical absorption map changes at each scanning step, which introduces inconsistency into the system equation [13], the design improves the light intensity around the region of focus and allows for imaging a larger object. The data acquisition (DAQ) unit used in the updated system has 128 channels (Vantage-128, Verasonics Inc.) and the acquisition speed is two times faster than the original system with a 64-channel DAQ unit. Acoustic signals are detected by a 128-element linear transducer array (ATL/Philips L7-4) with 5 MHz central frequency, 3.8 cm lateral length, and 2.5 cm elevation focus. For scanning a 3.8 cm × 4 cm region at a 0.1 mm step size, the entire experiment took 40 seconds. The digitized photoacoustic signals were then reconstructed through a focal-line-based algorithm that treats the slit as a virtual line detector to calculate the acoustic time of arrival between each acoustic transducer and reconstruction point [11, 14]. The reconstructed image represents the product of optical absorption and fluence. For better visualization, the reconstructed 3D image was projected along the axial direction of transducer array to form a depth-encoded MIP (Max Intensity Projection) image. Table 1 summarizes the major differences between the two systems.

3. Results

To test the effect of different slit widths, we first imaged a leaf phantom. The phantom was placed at 4 cm away from the slit to ensure a large elevation coverage (the diffraction far field). The energy on the leaf phantom's surface was 15 mJ/cm^2. An area of 3.8 cm × 4 cm was scanned along the elevation direction (z axis, Fig. 2a). Figure 2 shows maximum intensity projected (MIP) images acquired at different slit widths. It can be seen that as the slit width increases, the image becomes blurry along the elevation (z) direction. For instance, in Fig. 2b, both the midrib, primary veins and secondary veins are distinctly resolved, and the features look very similar to the leaf photograph (Fig. 2a). Fig. 2c still resolves features of the midrib and primary veins because of their large diameter, but the secondary veins become blurry due to the decreased resolution. Fig. 2d provides the most blurry image due

to its largest slit width. Only the midrib looks as sharp as other images. To quantify the elevation resolution, we chose a small leaf vein growing along the elevation direction (red arrow, Fig. 2a). The diameter of this vein is approximately 200 μm, which is less than the smallest slit width. For each slit width, we identified the vein in the 3D dataset and quantified the resolution by calculating full width at half maximum (FWHM) along the elevation resolution. The results are shown in Table 2. It can be seen that the resolutions are very close to the corresponding slit width. This result can be explained by the Fraunhofer diffraction theory which states that the diffraction angle θ is proportional to the ratio of wavelength (λ) and slit width (d): $\sin(\theta) \approx \lambda/d$. As the slit width increases, the diffraction angle of high frequency ultrasound signal (small λ) decreases, which, in term, reduces the elevation coverage and the corresponding spatial resolution. In this regard, the slit works as a tool to effectively control the receiving angle and frequency components along the elevation direction.

While an increased slit width degrades the spatial resolution, it improves the detected signal amplitude, because a larger slit allows more signals to pass through. In Figs. 2b–2d, the upper limit of the color bar corresponds to the maximum value in each image. It can be seen that changes in maximum intensity is close to the slit width ratio (1:2:3). We also quantified the signal to noise (SNR) ratio at different slit widths (Table 2). The area used to calculate SNR were identified by coloured boxes: the yellow box shows the area for signal calculation (average) while the green box indicates the area for noise calculation (standard deviation). Similar to the resolution study, the calculation was performed on the original 3D dataset. As expected, as the slit width increases, the SNR also increases (Table 2). These results indicate that, in order to reach an optimum balance between spatial resolution and SNR, the slit width should be chosen based on the object feature.

To test the imaging capability for structures distributed in 3D, we imaged a tube filled with black ink. The tube was embedded in an agar gel (3% in weight) whose optical scattering property mimics that of breast tissue (Fig. 3a) [15–17]. Inside the gel, the tube was twisted to form a structure in 3D. Because the tube has an inner diameter of 0.5 mm, we chose a slit width of 0.6 mm. To confirm the elevation resolution improvement, we also scanned the same phantom by conventional PAT without slit. In that experiment, the phantom's top surface was located near the transducer focus (25 mm), where the transducer had the highest elevation resolution. Fig. 3b and Fig. 3c are depth-encoded images of tube phantom reconstructed by conventional PAT and slit PAT, respectively. It can be clearly seen that in Fig. 3b the tube looks blurry along the elevation direction (z) and the blurriness increases as the tube is further away from the elevation focus (increased relative depth). In contrast, the tube in Figs. 3c and 3d looks very clear and the elevation diameter remains the same at different depths. We also quantified the elevation resolution at three tube cross sections, as identified by arrows with different colors (Fig. 3). The average resolution of slit PAT is 0.64 mm, which is close to the 0.60 mm slit width. For conventional PAT, the average resolution is 1.50 mm. Thus slit-PAT improves the elevation resolution by at least two times. These data also revealed that the slit technique works well over a large axial depth of over 25 mm.

To demonstrate the *in vivo* imaging capability of our updated system, we imaged the palms of two volunteers. All human imaging studies were performed in compliance with the

University at Buffalo IRB protocol. An area of 3.8 cm × 4 cm was imaged as indicated by red boxes in Figs. 4a and 4d. For the second volunteer, there is a nevus located near the bottom right corner of the scanning area, as identified by a white arrow. The energy on the skin surface was 27 mJ/cm^2, which is much lower than the ANSI safety limit of 100 mJ/cm^2 [18]. We set a slit width of 600 μm for imaging vessels with close to or larger than 600 μm diameter. The depth encoded results are shown in Figs. 4b and 4e. Rich vascular structures can be clearly seen in both images. For the second volunteer, the nevus can also be identified in the photoacoustic image (white arrow, Fig. 4e). The depth encoded color indicates that our technique can clearly resolve features distributed over 15 mm in depth. Such a performance could not be acquired by conventional linear-array-based PAT. For better illustration, 3D volume images are shown in Figs. 4c and 4f.

We further imaged the forearm of two volunteers to validate that our updated system can image larger vessels. The scanning size and optical intensity were set to be the same as the previous hand experiment. We increased the slit width to 900 μm because the forearm vessels are larger than that of the palm. The red boxes in Figs. 5a and 5d indicate the imaged regions for volunteer 1 and 2, respectively. No blood vessels could be identified in photographs due to light scattering. In contrast, the PA images (Figs. 5b and 5e) clearly show vessels at various depths. Compared to palm images where vessels are small and densely distributed, the arm vessels are much larger and more sparsely distributed. Because the imaged region of the arm was flatter than that of the palm, the relative depth of blood vessels in the arm ranged from 0~10 mm, while the palm vessels ranged from 0~15 mm depths. Again, for better illustration, we generated 3D volumetric images shown in Figs. 5c and 5f.

4. Discussion and conclusion

In conclusion, we improved our original slit PAT system to achieve faster imaging speed and more convenient clinical imaging. Performance of the system was demonstrated through both phantom and human studies. High-resolution vascular images of human palm and forearm were acquired with different slit widths. The images show uniform spatial resolution over the entire reconstruction volume, demonstrating potential for clinical imaging of tumor angiogenesis [19] or vascular disorders in the upper extremities [20]. Compared to other techniques to improve elevation resolution in a linear array, our method possesses the highest imaging speed with the best spatial resolution. Compared to vascular PAT systems based on custom-made arrays [21], our system uses a widely available clinical transducer array and a simpler scanning method, which will ensure faster clinical adoption. Future improvements can be made to increase the lateral field of view, to further improve the imaging speed, and to incorporate ultrasound imaging. For instances, a Philips L12-5-50 mm array will increase the lateral coverage from 38 mm to 50 mm. The Vantage 256 system has two transducer connectors and can potentially double the lateral length to 10 cm, which will be sufficient to cover the whole hand. High speed 100 Hz lasers (e.g., Lab-190, Spectra-Physics) are available and can be used to shorten the imaging time to by ten times. The slit principle can also be applied in ultrasound to achieve dual-mode imaging. Implementing these improvements will allow us to build a high speed and high resolution vascular and structural imaging system for clinical use.

Acknowledgments

This work was sponsored in part by the University at Buffalo Startup Fund, the IMPACT award, the SUNY Brain Network of Excellence “Big Idea” Award, and NIH R21EY026411.

References

1. Needles A, Heinmiller A, Sun J, Theodoropoulos C, Bates D, Hirson D, Yin M, Foster FS. IEEE Trans. Ultrason., Ferroelect., Freq. Control. 2013; 60(5):888–897.
2. Garcia-Uribe A, Erpelding TN, Krumholz A, Ke H, Maslov K, Appleton C, Margenthaler JA, Wang LV. Sci. Rep. 2015; 5:15748. [PubMed: 26510774]
3. Song L, Maslov K, Bitton R, Shung KK, Wang LV. J. Biomed. Opt. 2008; 13(5):054025–054028. [PubMed: 19021405]
4. Gateau J, Chekkoury A, Ntziachristos V. J. Biomed. Opt. 2013; 18(10):106005. [PubMed: 24096299]
5. Schwarz M, Buehler A, Ntziachristos V. J. Biophotonics. 2015; 8(1–2):60–70. [PubMed: 24733816]
6. Li G, Xia J, Li L, Wang L, Wang LV. SPIE BiOS. 2015; 9323:93230I. pp.
7. Li G, Li L, Zhu L, Xia J, Wang LV. J. Biomed. Opt. 2015; 20(6):066010. [PubMed: 26112369]
8. Gateau J, Caballero MÁA, Dima A, Ntziachristos V. Med. Phys. 2013; 40(1):013302. [PubMed: 23298121]
9. Gateau J, Gesnik J-M, Chassot M, Bossy E. J. Biomed. Opt. 2015; 20(5):056004.
10. Wang D, Wang Y, Zhou Y, Lovell JF, Xia J. Biomed. Opt. Express. 2016; 7(5):1957–1965. [PubMed: 27231634]
11. Wang Y, Wang D, Zhang Y, Geng J, Lovell JF, Xia J. Opt. Lett. 2016; 41(1):127–130. [PubMed: 26696175]
12. Michaud M, Leong T, Swiergon P, Juliano P, Knoerzer K. Ultrason. Sonochem. 2015; 26:56–63. [PubMed: 25637292]
13. Lou Y, Nadvoretskiy V, Wang K, Emilov S, Oraevsky A, Anastasio MA. SPIE BiOS. 2015; 9323:93233L. pp.
14. Xia J, Guo Z, Maslov K, Aguirre A, Zhu Q, Percival C, Wang LV. J. Biomed. Opt. 2011; 16(9): 090503–090505.
15. Pogue BW, Patterson MS. J. Biomed. Opt. 2006; 11(4):041102–041116. [PubMed: 16965130]
16. Cubeddu R, Pifferi A, Taroni P, Torricelli A, Valentini G. Phys. Med. Biol. 1997; 42(10):1971. [PubMed: 9364593]
17. Jacques SL. Phys. Med. Biol. 2013; 58(11):R37. [PubMed: 23666068]
18. American national standard for the safe use of lasers. American National Standards Institute; 2000.
19. Heijblom M, Klaase JM, van den Engh FM, van Leeuwen TG, Steenbergen W, Manohar S. Technol Cancer Res T. 2011; 10(6):607–623.
20. Zimmerman N. Hand Clin. 1993; 9(1):139–150. [PubMed: 8444972]
21. Kruger RA, Kuzmiak CM, Lam RB, Reinecke DR, Del Rio SP, Steed D. Med. Phys. 2013; 40(11): 113301. [PubMed: 24320471]

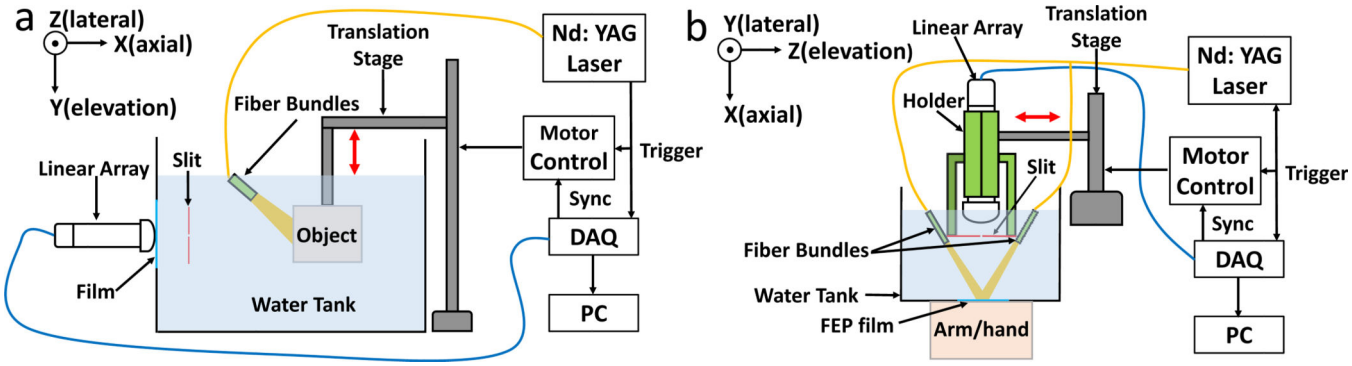

Figure 1.

Schematics of slit-based PAT systems. (a) The original slit PAT system. (b) The updated slit PAT system. For both systems, the slit is placed at the transducer array focus (25 mm). The red double arrows indicate the scanning direction.

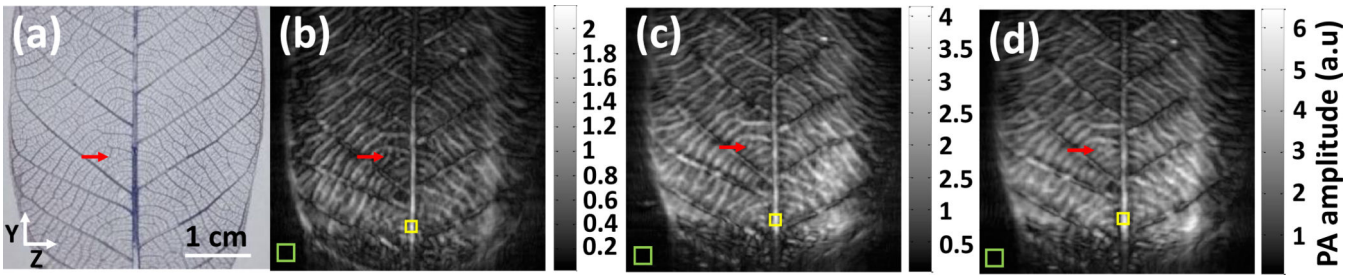

Figure 2.

Leaf phantom experiment performed at different slit widths. (a) Real leaf phantom image. (b) MIP image of 3D data acquired with 300 μm slit width. (c) MIP image of 3D data acquired with 600 μm slit width. (d) MIP image of 3D data acquired with 900 μm slit width. Red arrows identify the leaf vessel used for resolution calculation. Green boxes indicate the area for signal intensity calculation, and yellow boxes indicate the area for noise intensity calculation.

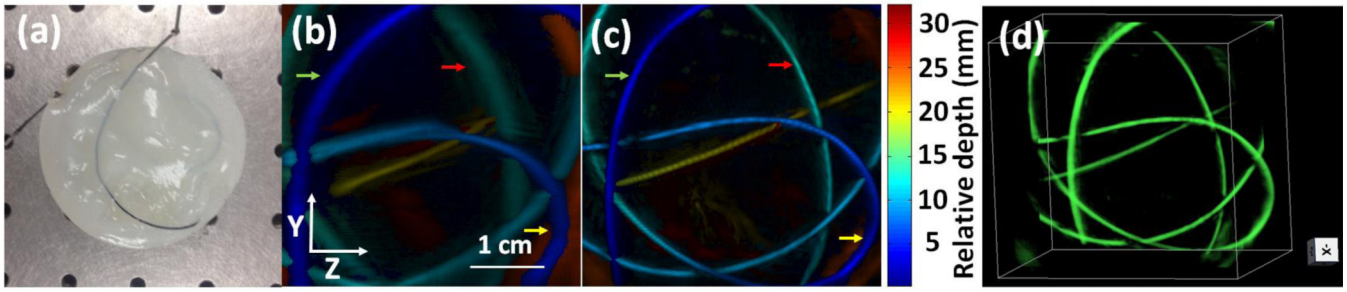

Figure 3.

Tube phantom experiment. (a) Photograph of the tube phantom. (b) Depth-encoded image of the tube phantom reconstructed by PAT. (b) Depth-encoded image of the tube phantom reconstructed by slit PAT. (d) Slit PAT 3D reconstructed images of the tube phantom. Arrows identify the tube section used for resolution quantification.

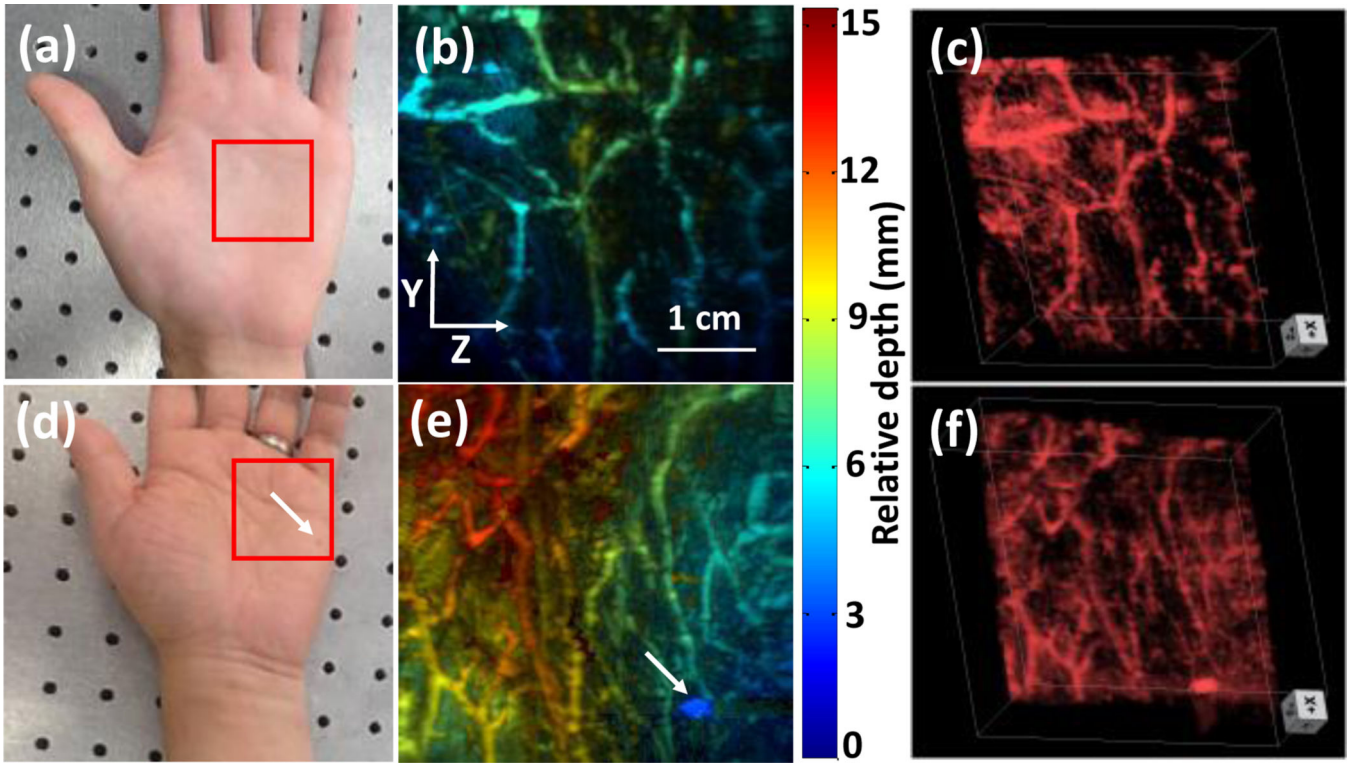

Figure 4.

Palm experiment. (a) Photograph of the palm of volunteer 1. (b) Depth-encoded palm vascular image of volunteer 1. (c) 3D palm vascular images of volunteer 1. (d) Photograph of the palm of volunteer 2. (e) Depth-encoded palm vascular image of volunteer 2. (f) 3D palm vascular images of volunteer 2. Red boxes indicate the scanning region.

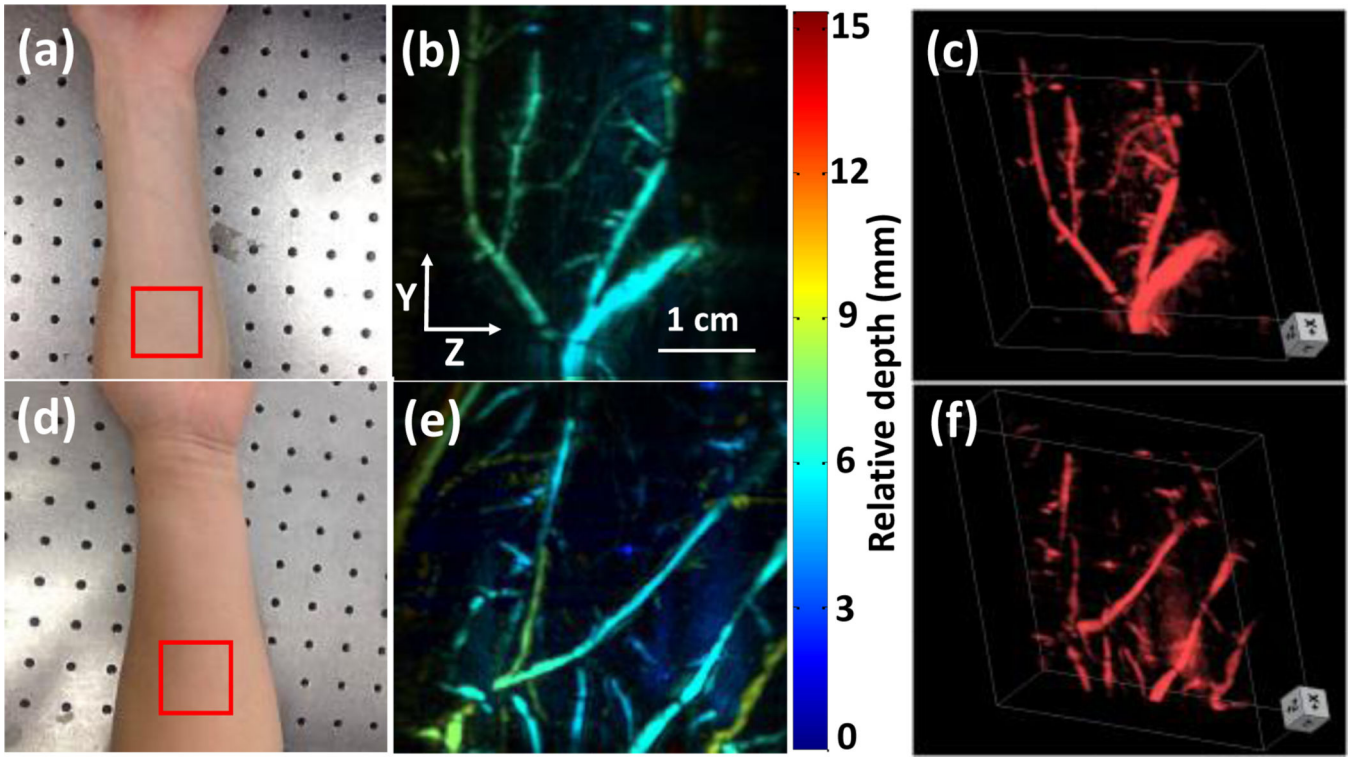

Figure 5.

Forearm experiment. (a) Photograph of the forearm of volunteer 1. (b) Depth-encoded forearm vascular image of volunteer 1. (c) 3D forearm vascular images of volunteer 1. (d) Photograph of the forearm of volunteer 2. (e) Depth-encoded forearm vascular image of volunteer 2. (f) 3D forearm vascular images of volunteer 2. Red boxes indicate the scanning region.

Table 1

Major differences between the first and second generation slit-PAT systems.

	Scanning method	Light delivery	Slit size	DAQ
Original system	Vertically scan the object	Single circular fiber bundle illuminating a fixed location	Fixed (300 um)	64 channels
Updated system	Horizontally scan the transducer and the slit together	Two line fiber bundles moving simultaneously with transducer array	Adjustable	128 channels

Table 2

Elevation resolution and SNR analysis of different slit widths.

Slit width	300 micron	600 micron	900 micron
Resolution	0.35 mm	0.64 mm	0.89 mm
SNR	5.76	7.17	9.41

Table 3

Elevation resolution analysis of PAT and slit PAT.

	Green arrow	Red arrow	Yellow arrow	Average resolution
600 micron slit	0.66 mm	0.58 m	0.69 mm	0.64 mm
No slit	1.28 mm	1.65 mm	1.41 mm	1.50 mm